University of Pennsylvania
ScholarlyCommons

Departmental Papers (MEAM)

Department of Mechanical Engineering & Applied Mechanics

October 2004

Molecular Dynamics Simulation of Thermal Conduction in Nanoporous Thin Films

Jennifer R. Lukes
University of Pennsylvania, jrlukes@seas.upenn.edu

C. L. Tien
University of California, Berkeley

Follow this and additional works at: http://repository.upenn.edu/meam_papers

Recommended Citation
Lukes, Jennifer R. and Tien, C. L., "Molecular Dynamics Simulation of Thermal Conduction in Nanoporous Thin Films" (2004). *Departmental Papers (MEAM)*. Paper 60.
http://repository.upenn.edu/meam_papers/60

Postprint version. Published in *Microscale Thermophysical Engineering*, Volume 8, Issue 4, October/November/December 2004, pages 341-359.
Publisher URL: http://dx.doi.org/10.1080/10893950490516893

This paper is posted at ScholarlyCommons. http://repository.upenn.edu/meam_papers/60
For more information, please contact repository@pobox.upenn.edu.

Molecular Dynamics Simulation of Thermal Conduction in Nanoporous Thin Films

Abstract
Molecular dynamics simulations of thermal conduction in nanoporous thin films are performed. Thermal conductivity displays an inverse temperature dependence for films with small pores and a much less pronounced dependence for larger pores. Increasing porosity reduces thermal conductivity, while pore shape has little effect except in the most anisotropic cases. The pores separate the film into local regions with distinctly different temperature profiles and thermal conductivities, and the effective film thermal conductivity is lowest when the pores are positioned in the center of the film. Such tunability by pore placement highlights new possibilities for engineering nanoscale thermal transport.

Keywords
Molecular Dynamics, Nanopore, Thin Film, Local Thermal Conductivity, Tunable Properties

Comments
Postprint version. Published in *Microscale Thermophysical Engineering*, Volume 8, Issue 4, October/November/December 2004, pages 341-359.
Publisher URL: http://dx.doi.org/10.1080/10893950490516893

This journal article is available at ScholarlyCommons: http://repository.upenn.edu/meam_papers/60

Molecular Dynamics Simulation of Thermal Conduction in Nanoporous Thin Films

J. R. Lukes[1]
Department of Mechanical Engineering and Applied Mechanics
University of Pennsylvania
Philadelphia, Pennsylvania 19104-6315
Tel: 215-898-3254
Fax: 215-573-6334
jrlukes@seas.upenn.edu

C. L. Tien[2]
Department of Mechanical Engineering
University of California
Berkeley, California 94720

Abstract

Molecular dynamics simulations of thermal conduction in nanoporous thin films are performed. Thermal conductivity displays an inverse temperature dependence for films with small pores and a much less pronounced dependence for larger pores. Increasing porosity reduces thermal conductivity, while pore shape has little effect except in the most anisotropic cases. The pores separate the film into local regions with distinctly different temperature profiles and thermal conductivities, and the effective film thermal conductivity is lowest when the pores are positioned in the center of the film. Such tunability by pore placement highlights new possibilities for engineering nanoscale thermal transport.

Introduction

Nanoporous thin film materials such as xerogel intermetal layers for high-speed microelectronic devices [1] and high surface area chemical sensors [2] possess physical

[1] To whom correspondence should be addressed

[2] Deceased October 29, 2002

properties far different from those of solid bulk materials. The unusual optical, electrical, thermal, mechanical, and chemical characteristics of these materials arise from the extremely small dimensions of their solid matrix and pores and from their enormous surface area per unit volume. Nanometer-scale pores also occur in materials that are not normally considered porous. Thin "solid" films, for instance, often contain voids that arise during the film deposition process [3]. These voids assume a variety of shapes, including irregular triangular and circular pinholes [4], cylindrical pipes [5], and pyramidal defects [6]. Thermal conductivity reduction caused by the presence of pores/voids often results in higher hot spot temperatures than for defect-free films. Severe performance problems or even failure, for example the accelerated breakdown of thin oxide layers in VLSI devices [7] or thermomechanical damage of optical thin films [8], can result at such elevated temperatures. It is thus critically important for device design purposes to understand the influence of nanometer-scale pores on the conduction of heat in thin films.

Thermal conduction in porous media has historically been treated using several methods, including simple arithmetic and geometric mixing rules, effective medium approximations, and statistical analyses [9; 10]. One drawback of such methods is that they require idealized geometrical assumptions. Finite-difference [11] and finite element modeling can handle complex structural configurations, but do not account for the thermal conduction size effects [12] that often arise in confined geometries such as the solid matrix surrounding the pores. Chung and Kaviany [13] applied the Boltzmann transport equation to a two-dimensional grid of occupied (solid) and unoccupied (pore) sites in their study of porous silicon thermal conductivity and found a significant size effect. It is of interest, however, to study systematically the effects of temperature and pore configuration and to include the effect of the third dimension, which is a critical pathway for thermal conduction. Classical molecular dynamics (MD) simulation, which

inherently accounts for size effects and easily incorporates pores of any configuration, is a computationally tractable approach employed by several groups (for example [14-16]) to study nanoscale solid materials.

For the above reasons, three dimensional MD simulations on nanoscale porous thin films are performed in the present study to investigate the effects of average lattice temperature, pore size, pore shape, and pore arrangement on thermal conduction. The well known Lennard-Jones (LJ) argon model is used. The particular shapes and configurations used in the current study were chosen because they occur in thin film materials or are expected to offer some new insight into thermal conduction in thin porous films. The pores simulated range from single atomic vacancies to voids about 2 nm in size.

General comments about the simulations

The computational setup, thermal conductivity calculation, and error calculation procedure found in Lukes et al. [17] are employed in the present simulations. Thermal conductivity is calculated by imposing a heat flux at the hot and cold boundaries of the films, performing a linear fit to the resultant temperature gradient across the atoms, and taking the ratio of flux to temperature gradient. The heat flux is imposed using an algorithm that adjusts the atomic velocities such that a fixed amount of energy is added to the hot atoms and removed from the cold atoms [18] at every time step. The imposed flux must be high enough to yield suitably low error in the temperature profiles yet low enough to prevent the unphysical situation of removing more energy than that contained within the cold region. It was found that the dimensionless flux value of 0.3 was sufficient to balance these competing requirements for a wide variety of film temperatures, so this value was used for most runs.

Pores are created by removing selected atoms from lattice sites near the center of the films to create vacancies and vacancy clusters (pores/voids). Figure 1 illustrates the computational configuration, where the term "regular" indicates the atomic region between the hot and cold boundaries whose thermal conductivity is being measured. The number and location of the vacancies determine the size and shape of the pores as well as the configuration of the porous thin film. Fixed-wall boundary conditions are used in the x (cross-plane) direction. Boundaries such as these may be encountered in devices where a thin film is sandwiched between other layers of much higher stiffness or much lower thermal expansion coefficient. Periodic boundary conditions are used in the y- and z-directions. Parameters and standard nondimensionalizations used in the simulations are given in Table 1.

Certain considerations, as compared to the fully dense thin film case, arise due to the presence of the pores. For example, the one-dimensional thermal conductivity calculation approach described in the preceding paragraphs is admittedly somewhat crude because it neglects three-dimensional effects of flow around the pores and the effects of locally varying temperature profiles; these effects are discussed further in the final section of the paper. The 1D approach, however, is useful for engineering estimation as a simplified and consistent method to handle the variety of pore configurations in the present work. As a check on the utility of this method of thermal conductivity calculation, the absolute temperature difference across the film was also calculated (Fig. 7) as an alternative indicator of the ease of heat conduction. As expected, the temperature difference values consistently support the thermal conductivity values: when effective thermal conductivity is the lowest the temperature difference is always highest and vice versa. The "effective" thermal conductivity calculated here should thus be regarded as a qualitative indicator rather than a precise value.

Also, randomly removing more than about 10% of the atoms from their lattice sites at the dimensionless average film temperature $T^* = 0.50$ causes the crystal to begin to melt, and removing more than 20% results in a completely fluid phase due to the reduction in density. Additionally, migration of surrounding atoms into, around, and across the pores at lower vacancy concentrations occurs above $T^* = 0.29$. The initial/final snapshots of Fig. 2 illustrate atomic migration and the resultant pore relaxation at $T^* = 0.50$. Near-pore relaxation occurs because the lack of atomic repulsion from within the pore allows the surrounding atoms to move and assume energetically more favorable positions. This effect becomes more pronounced with increasing pore size. At higher temperatures, thermophoretic migration of a few atoms from the warmer to the colder side of the film occurs.

The hot and cold bath atoms are tethered to their original lattice sites with simple harmonic springs to prevent diffusion into the regular atoms. The use of springs to maintain the integrity of atomic walls is common practice in MD simulations (see Murad et al. [19]). The spring constant chosen was roughly one-fifth that obtained by evaluating the second derivative of the LJ potential at the equilibrium point at the bottom of the potential well. This value was used because it yields forces of the same order as those exerted by the surrounding atoms.

Simulations were run at a variety of temperatures, film thicknesses, and pore sizes to observe the effects of tethering, cross-sectional (y-z) location of the pore, imposed heat flux, and total time steps on thermal conductivity. The data from these simulations [20] indicate that varying the above parameters does not, within error, cause any significant change in conductivity.

Dependence of thermal conductivity on temperature

Experimental data compiled by Cahill et al. [21] indicate that increasing dopant concentration in a crystal causes the thermal conductivity temperature dependence to change from that characteristic of crystalline materials to that of amorphous materials unless the doping is a simple monatomic substitution of an atom from the same group in the periodic table. In the latter case the classical crystalline inverse temperature dependence is maintained regardless of doping level. This behavior arises from the dominance of Umklapp phonon-phonon scattering at high temperatures [34]. Essentially, the doping strongly reduces the peak thermal conductivity, leading to a much less pronounced temperature dependence at high temperatures. Experimental data on radiation-damaged crystals [22-24] also show a substantial flattening of the temperature dependence of thermal conductivity. Molecular dynamics simulations of doped bulk crystals in the literature [25-27] are consistent with these experimental trends at temperatures on the order of or above the Debye temperature. It is expected that thin films "doped" with pores will show similar behavior.

To investigate this, simulations were run for thin films with pores of differing sizes and temperatures. The temperatures studied are in the classical regime, which, as indicated in the thermal conductivity measurements of White and Woods [28] and Clayton and Batchelder [29], is above 20 K ($T^* = 0.15$), or about one-fourth the Debye temperature of argon. The general configuration for this set of simulations was a single planar square void in the middle plane of a film 7 regular x-planes thick with a 4x4 cross section. Here x-plane indicates an atomic layer of atoms perpendicular to the x (cross-plane) direction and 4x4 indicates that the cross section of the film is composed of 4 face centered cubic unit cells in the y- and z-directions.

In contrast to results from simulations of bulk β-SiC [25], which show a dramatic jump between inverse and flat thermal conductivity temperature dependence with the addition of a single vacancy defect, the present thin film results (Fig. 3) display a gradual change between these two regimes as pore size increases. The onset of temperature-independent thermal conductivity, however, occurs in a similar vacancy concentration range for both cases (0 - 0.5% [25]; 0.2 - 1.2% present results). This behavior is consistent with experimental data on doped and defective crystals discussed above. For the solid thin film case (*0 vac*), thermal conductivity is noticeably lower than the experimental bulk values (*exptl bulk*) [30] for the entire temperature range shown and has a weaker temperature dependence. These effects are attributed to the increased effects of boundary scattering, which reduces the peak thermal conductivity. Adding a single vacancy defect to the middle of the thin film (*1 vac*) further reduces thermal conductivity and weakens the temperature dependence, but monotonically decreasing thermal conductivity with increasing temperature is still observed. Increasing the vacancy cluster size to 5 and 9 vacancies (*5 vac*, *9 vac*), however, reveals an almost flat dependence that appears to decrease slightly at higher temperatures. The theoretical lower limit of thermal conductivity (k_{min}) [21] for argon, calculated using the temperature-dependent transverse and longitudinal speeds of sound [31] and the *0 vac* simulation density, bounds the simulation data nicely and demonstrates flat behavior at higher temperatures.

The introduction of vacancy defects increases structural disorder in the thin film. Figure 4 shows that this disorder becomes more pronounced with increasing temperature and pore size. The flat behavior observed at lower temperatures for the *5 vac* and *9 vac* cases indicates that the disorder is strong enough so that defect scattering dominates, while the slight decay at higher temperatures indicates that Umklapp scattering is again becoming important in this regime.

Dependence of thermal conductivity on pore size and configuration

Several simulations were run to analyze the effect of pore size and configuration on thermal conductivity. It is expected that there should be some effects of shape, arrangement, and orientation relative to heat flow direction, as has been demonstrated in studies on fibrous composites [35] and random packed beds [36]. The present configurations include square and hexagonal planar voids similar to the nearly flat pinholes found in $CoSi_2$ [4], cubic pores, pyramidal pores like those occurring in SiC [6], and cylindrical pipe-like voids resembling those in GaN [5] and SiC. Also studied were systems with two pores of differing sizes as well as systems with a number of randomly distributed vacancies. Most of the films studied in this section were 9 regular x-planes thick with a 6x6 cross section at $T^* = 0.50$. The effect of increasing vacancy number was investigated in the planar, cubic, and pyramidal cases by removing atoms in equal proportions from all edges of the pore, in the cylindrical cases by elongating the pore, and in the random cases by distributing more vacancies throughout the volume of the film. To elucidate the effect of uneven vacancy distribution on thermal conduction, the pore sizes in the two-pore cases were systematically varied while maintaining a constant total vacancy number of 30. Figure 5 illustrates the various pore configurations in greater detail.

The dependence of thermal conductivity on vacancy fraction (ϕ_v) for the above cases is shown in Fig. 6, along with experimental values for bulk solid argon [29] at their corresponding molar volumes: 22.53 and 23.35 mL/mol correspond to 0.000 and 0.035 vacancy fraction, respectively. All values in Fig. 6 are normalized by their fully dense (22.53 mL/mol) thermal conductivity values. Also shown is a simple parallel effective conductivity estimate for the

simulation cell using a pore thermal conductivity of zero. A series model is not shown as it gives zero values of thermal conductivity for all vacancy fractions greater than zero. As they fall below the parallel limit, the simulation results are thus bounded, albeit not closely, by the two simple thermal conductivity models for porous materials. In general, thermal conductivity decreases with increasing vacancy fraction and has, in general, little dependence on pore shape, orientation, or configuration for the cases examined. The functional form of this dependence is quite similar to that observed in MD thermal conductivity simulations of bulk diamond with vacancies [37], and the exponent is almost identical (0.68 for the present data; 0.69 in [37]). Within error, most of the configurations fall within a single envelope that appears to broaden as vacancy faction increases. The reason for the absence of strong configuration effect is not that all pores relax to the same shape: no conclusive similarity among the final pore shapes for these configurations was observed. Instead, it is likely that most pores are not anisotropic enough to register strong configuration effects. Only the most anisotropic pores simulated, 4x1x1 unit cell cylindrical pores at 0.038 vacancy fraction oriented parallel (*cyl*-||) and perpendicular to (*cyl-prp*) the heat flow direction, show a clear configuration effect.

It is also seen in Fig. 6 that the *pl-sq-7p* point at 0.021 vacancy fraction, which corresponds to a 7 regular x-plane film with 4x4 cross section, lies near the low edge of the thermal conductivity envelope. As the other envelope points are for thicker (9 x-plane) films, this result may indicate that vacancy fraction dependence is stronger in thinner films or films with smaller cross sections. As the characteristic dimensions of the solid matrix surrounding a single central pore will in general be smaller for such films than for thicker/larger cross section films or bulk materials at the same vacancy concentration, this stronger dependence could arise from enhanced size effects [17], in the surrounding matrix as pore size increases. This idea is

supported by comparison to the scant bulk experimental data available, which show a weaker dependence on density than the simulated thin film cases. As the *pl-sq-7p* value is not clearly outside the envelope, however, conclusive determination of film thickness and/or cross section effects cannot be made.

Dependence of temperature profile, thermal boundary resistance, and thermal conductivity on pore location

A series of simulations run for 3 million timesteps using an 11 regular x-plane, 4x4, 5 vacancy square planar pore configuration at the average film temperature $T^* = 0.17$ reveals a surprising trend. For each simulation, the pore was placed in a different location relative to the hot and cold boundaries. An additional simulation without the pore was run under the same conditions to provide a basis for comparison. A plot of temperature profile versus x-planar position of the pore and the corresponding schematic drawing of the pore's position is shown in Fig. 7. The first number in the lower left corner of each plot indicates the x-plane of the pore, with "1" and "11" indicating that the pore is in the left- and right-most regular x-planes, respectively. The second number indicates the dimensionless temperature difference across the film. The two horizontal lines in each plot highlight the temperature jump between the planes immediately adjacent to the pore. The small dashes at either end of each temperature profile represent the temperatures of the innermost layers in the hot and cold regions adjoining the regular atoms.

Figure 7 shows that the regions on either side of the pore exhibit two different, essentially linear temperature profiles when the pore is not equidistant from the boundaries. At the pore, there is a clear temperature jump, and in certain cases very slight jumps also appear at the hot

and cold boundaries of the film [20]. The temperature jumps observed in the present simulations are less pronounced than those found by Kotake and Wakuri [38]. This is likely due to the two-dimensional nature of their simulations, which disallows the additional heat flow pathways in the third dimension available in the present simulations.

The "thermal boundary resistance" induced by the pore can be estimated by dividing the temperature jump across the pore by the applied heat flux. Quotation marks are used to emphasize that the present case does not involve the usual case of conduction between two different media across a perfect interface but rather across a porous region embedded in a single medium. Figure 8 illustrates the dimensionless thermal boundary resistance for the various cases as a function of planar pore position. As the pore progresses across the film from the hot (left) side to the cold (right) side, the pore resistance first decreases noticeably, then decreases almost imperceptibly, maintaining dimensionless values in the range $R^* \sim 0.11$, then increases again. This value corresponds to a dimensional thermal boundary resistance of 2×10^{-9} K-m^2/W, which, for comparison, is about an order of magnitude smaller than the resistance between gold and silicon dioxide measured by Young et al. [39]. The present simulations do not display the clear monotonic increase in thermal boundary resistance with decreasing temperature that would be expected at interfaces between solid materials [40; 41]. This could be a result of the nonideal porous 'interface,' the high (classical) temperatures being simulated, and/or the effect of the hot and cold boundaries near the pore. Figure 8 also shows that in general, the pore thermal boundary resistance represents about 30% of the total thermal resistance of the film, although the fraction approaches the 40-50% range for pores near the boundaries. As the pore approaches the boundaries, the increase in effective thermal conductivity (see discussion below) leads to a

decrease in film resistance. This, in combination with the slightly increasing pore resistance near the boundaries, leads to the increased contribution of the pore to the overall film resistance there.

Effective thermal conductivity versus position of the pore is shown in Fig. 9 for the above simulations (*T*=0.17,5vac,11pl*) and for other related cases. It is seen that the effective thermal conductivity of the film is symmetric with respect to pore position, with the lowest thermal conductivity occurring when the pore is in the center of the film. Comparison of $T^* = 0.17$, 7 x-plane films with 1 and 5 vacancies (*T*=0.17,1vac,7pl*, *T*=0.17,5vac,7pl*) shows that the variation of thermal conductivity with respect to pore position is significantly stronger for larger pores. The variation in conductivity is less pronounced for thicker films, as is seen by comparing $T^* = 0.17$, 5 vacancy films that are, 7 and 11 x-planes thick (*T*=0.17,5vac,7pl*, *T*=0.17,5vac,11pl*). This is likely caused by the smaller influence of the boundaries for the thicker films. Increasing the temperature to 0.29 for the 1 vacancy 7 plane case yields a consistent decrease in conductivity; this effect is less pronounced than the film thickness and pore size changes above. Simulations of both 1.5 and 3 million time steps (*T*=0.17,5vac,11pl,1.5mil*, *T*=0.17,5vac,11pl*) indicate no time dependence in the results. Also, no time dependence was observed for the other cases in Fig. 9. This indicates that the unusual two-slope temperature profile is a repeatable, steady state phenomenon.

The dependence of temperature profile, thermal boundary resistance, and effective thermal conductivity on pore position is an unexpected result and it is of interest to analyze the local planar temperatures and heat fluxes of the regular atoms to try to gain insight into this behavior. Figures 10-12 show the local heat fluxes (arrows) and temperatures (contour lines) for 5-vacancy flat pores near the hot end (Fig. 10), center (Fig. 11), and cold end (Fig. 12) of the film at $T^* = 0.17$. The pores are slightly off center in the x-plane due to the FCC configuration;

as discussed above, this will have negligible effect on the calculations due to the periodic boundary conditions. The local values come from the time averaged temperatures of each atom. Each row or column represents an atomic plane. Temperatures in between the FCC lattice positions, which are needed in order to form a uniform grid for plotting, are calculated by spatially averaging the temperatures of the neighboring atoms. Although instantaneous temperature at a single atom is not meaningful, sufficient time averaging yields smooth, physically reasonable contours, as shown in the figures. In each figure, lengthwise ((a)-(c)) and cross-sectional ((d)-(f)) slices are taken from the film. Darkened vacancies indicate that the plane of interest intersects those vacancies. Slice (a) represents the y-plane just in front of but not including the pore, slice (b) contains two of the five vacancies and is the front-most y-plane intersecting the pore, slice (c) intersects the center of the pore and contains one of the five vacancies, slice (d) is the x-plane not containing but immediately adjacent to the pore on the hot side, slice (e) is the x-plane containing the pore, and slice (f) is the x-plane not containing but immediately adjacent to the pore on the cold side. Other x-, y-, and z-planes are not shown as they do not yield information materially different than that shown in Figs. 10-12.

The most dramatic characteristic in the figures is that steep contours are formed in the vicinity of each of the five vacancies comprising the pore ((b),(c),(e)). The steepness of the contours and the magnitude of the heat flux vectors in these regions should be viewed with some skepticism, however, as they are derived from a continuum representation. Interpreted in this perspective, the vacancies are regions of zero temperature and for this reason thermal energy flows toward them. In reality there are no ultracold locations but rather regions of lower density, and for this reason an atomistic representation is more meaningful. From this perspective, each vacancy is a void, so as discussed above the neighboring atoms have a tendency to fill it in. In

either interpretation, part of the heat from the surrounding atoms flows into the vacancies ((b) and (c) from the x-direction, (e) within the x-plane from y- and z-directions), while the other part flows around the vacancies ((b),(c)). Some heat even flows straight from hot to cold between the vacancies without being diverted (b). At the cold ($T^* = 0.17$) temperature here the heat flow into the vacancies is not large enough to result in atomic migration, but at higher temperatures and/or substantially longer simulation times on the order of the characteristic atomic diffusion time, the convective heat flux contribution due to vacancy transport would need to be considered. It would be of interest in a future study to examine the local disturbances caused by impurity atoms rather than vacancies so that zero temperature regions would be eliminated and the continuum and atomistic descriptions could be fully consistent.

The region of disturbance of the temperature contour lines caused by the vacancies extends roughly 2 atomic planes to either side of the pore in the x-direction((b),(c)), but less than a single atomic plane in the y-direction (a). The cooler contours are pulled ahead (to the left) of the pore, leaving a 'wake' behind it (b). When the pore is near the hot (Fig. 10) or cold (Fig. 12) ends of the film, the disturbance region intersects the boundary, resulting in noticeable crowding of the contour lines in those regions even in planes not containing the pores (Fig. 10(a), left side; Fig. 12(a), right side) as compared to the case where the pore is the center of the film (Fig. 11(a)). This contour crowding behavior is consistent with the steeper temperature gradients in the narrower regions observed in Fig. 7. In these crowded regions the x-plane crosses several contours and displays a somewhat chaotic flow pattern (Fig. 10(d), Fig. 12(f)), while on the opposite side of these regions (Fig. 10(f), Fig. 12(d)), as well as on both sides of the pore when the pore is in the center of the film (Fig. 11(d),(f)), the x-plane contours display a much smoother, almost concentric ring pattern.

Figures 7-12 are important because they show that effective thin film thermal conductivity can be tuned by careful placement of pores or voids and that different local thermal conductivities and temperature profiles exist on either side of these pores. This discovery highlights new possibilities for engineering heat flow in nanoscale porous structures. Key requirements to observe such tuning experimentally will be the ability to generate pores in precise locations in a thin film and maintain structural stability in the face of near-pore atomic migration. Works on the formation of high aspect ratio parallel arrays of pores in porous silicon [42] and porous alumina [43] and on the stabilization of porous silicon's structure by low-temperature oxidation [44] demonstrate important progress related to these issues.

Conclusions

Thermal conduction in solid thin films with nanometer-scale pores and voids is a critical factor affecting the performance of materials and devices in a number of optical and electronic applications. This paper investigates thermal conduction in solid thin films with nanopores using Lennard-Jones argon model molecular dynamics simulations. The effects of average film temperature, and pore placement, shape, size, and orientation on thermal transport are examined. The results show that larger porosities and higher temperatures yield lower conductivity values. Pore shape and configuration do not significantly influence thermal conduction, and orientation effects are visible only for the most anisotropic cases studied. The results also reveal that as pore size increases, the thermal conductivity temperature dependence changes from roughly inverse to flat.

Interestingly, the proximity of a pore to the hot and cold boundaries of a few-nanometer thick film influences effective film thermal conductivity. Conductivity is lowest when the pore

is equidistant from hot and cold boundaries, and it increases symmetrically as the pore moves toward each boundary. The pore is observed to separate the film into two regions with distinctly different temperature profiles and thermal conductivities, indicating that the simple placement of a pore is enough to create new local properties different from those elsewhere in the film and different from those normally associated with the host material. This discovery highlights new possibilities for engineering heat flow in nanoscale porous structures.

References

1. J.-K. Hong, H.-S. Yang, M.-H. Jo, H.-H. Park and S.-Y. Choi, Preparation and Characterization of Porous Silica Xerogel Film for Low Dielectric Application, Thin Solid Films, vol. 308-309, pp. 495-500, 1997.
2. S. E. Létant, S. Content, T. T. Tan, F. Zenhausern and M. J. Sailor, Integration of Porous Silicon Chips in an Electronic Artificial Nose, Sensors and Actuators B, vol. 69, pp. 193-198, 2000.
3. M. Ohring, The Materials Science of Thin Films, Academic Press, Boston, 1992.
4. L. Ruan and D. M. Chen, Pinhole Formation in Solid Phase Epitaxial Film of $CoSi_2$ on Si(111), Applied Physics Letters, vol. 72, pp. 3464-3466, 1998.
5. W. Qian, G. S. Rohrer, M. Skowronski, K. Doverspike, L. B. Rowland and D. K. Gaskill, Open-Core Screw Dislocations in GaN Epilayers Observed by Scanning Force Microscopy and High-Resolution Transmission Electron Microscopy, Applied Physics Letters, vol. 67, pp. 2284-2286, 1995.
6. R. Scholz, U. Gösele, E. Niemann and F. Wischmeyer, Micropipes and Voids at β-SiC/Si(100) Interfaces: An Electron Microscopy Study, Applied Physics A, vol. 64, pp. 115-125, 1997.
7. K. F. Schuegraf and C. Hu, Effects of Temperature and Defects on Breakdown Lifetime of Thin SiO2 at Very Low Voltages, IEEE Transactions on Electron Devices, vol. 41, pp. 1227-1232, 1994.
8. A. H. Guenther and J. K. McIver, The Pulsed Laser Damage Sensitivity of Optical Thin Films, Thermal Conductivity, Laser and Particle Beams, vol. 7, pp. 433-441, 1989.

9. S. Torquato, Modeling of Physical Properties of Composite Materials, International Journal of Solids and Structures, vol. 37, pp. 411-422, 2000.

10. B. Gebhart, Heat Conduction and Mass Diffusion, McGraw-Hill, New York, 1993.

11. K. Bakker, Using the Finite Element Method to Compute the Influence of Complex Porosity and Inclusion Structures on the Thermal and Electrical Conductivity, International Journal of Heat and Mass Transfer, vol. 40, pp. 3503-3511, 1997.

12. C.-L. Tien and G. Chen, Challenges in Microscale Conductive and Radiative Heat Transfer, Journal of Heat Transfer, vol. 116, pp. 799-807, 1994.

13. J. D. Chung and M. Kaviany, Effects of Phonon Pore Scattering and Pore Randomness on Effective Conductivity of Porous Silicon, International Journal of Heat and Mass Transfer, vol. 43, pp. 521-538, 2000.

14. V. Yamakov, D. Wolf, M. Salazar, S. R. Phillpot and H. Gleiter, Length-Scale Effects in the Nucleation of Extended Dislocations in Nanocrystalline Al by Molecular-Dynamics Simulation, Acta Materialia, vol. 49, pp. 2713-2722, 2001.

15. S. G. Volz and G. Chen, Molecular Dynamics Simulation of Thermal Conductivity of Silicon Nanowires, Applied Physics Letters, vol. 75, pp. 2056-2058, 1999.

16. D. Qian, W. K. Liu and R. S. Ruoff, Mechanics of C-60 in nanotubes, Journal of Physical Chemistry B, vol. 105, pp. 10753-10758, 2001.

17. J. R. Lukes, D. Y. Li, X.-G. Liang and C.-L. Tien, Molecular Dynamics Study of Solid Thin-Film Thermal Conductivity, Journal of Heat Transfer, vol. 122, pp. 536-543, 2000.

18. T. Ikeshoji and B. Hafskjold, Non-equilibrium Molecular Dynamics Calculation of Heat Conduction in Liquid and through Liquid-Gas Interface, Molecular Physics, vol. 81, pp. 251-261, 1994.

19. S. Murad, P. Ravi and J. G. Powles, Anisotropic Thermal Conductivity of a Fluid in a System of Microscopic Slit Pores, Physical Review E, vol. 48, pp. 4110-4112, 1993.

20. J. R. Lukes, Molecular Dynamics Simulation of Thermal Conduction in Solid and Nanoporous Thin Films, Ph.D. thesis, University of California, Berkeley, California, 2001.

21. D. G. Cahill, S. K. Watson and R. O. Pohl, Lower Limit to the Thermal Conductivity of Disordered Crystals, Physical Review B, vol. 46, pp. 6131-6140, 1992.

22. M. Rohde, Reduction of the Thermal Conductivity of SiC by Radiation Damage, Journal of Nuclear Materials, vol. 182, pp. 87-92, 1991.

23. D. J. Senor, G. E. Youngblood, C. E. Moore, D. J. Trimble, G. A. Newsome and J. J. Woods, Effects of Neutron Irradiation on Thermal Conductivity of SiC-Based Composites and Monolithic Ceramics, Fusion Technology, vol. 30, pp. 943-955, 1996.

24. R. J. Price, Thermal-Conductivity of Neutron-Irradiated Pyrolytic Beta-Silicon Carbide, Journal of Nuclear Materials, vol. 46, pp. 268-272, 1973.

25. J. Li, L. Porter and S. Yip, Atomistic Modeling of Finite-Temperature Properties of Crystalline β-SiC. II. Thermal Conductivity and Effects of Point Defects, Journal of Nuclear Materials, vol. 255, pp. 139-152, 1998.

26. G. V. Paolini, P. J. D. Lindan and J. H. Harding, The Thermal Conductivity of Defective Crystals, Journal of Chemical Physics, vol. 106, pp. 3681-3687, 1997.

27. D. N. Payton, III, M. Rich and W. M. Visscher, Lattice Thermal Conductivity in Disordered Harmonic and Anharmonic Crystal Models, Physical Review, vol. 160, pp. 706-711, 1967.

28. G. K. White and S. B. Woods, Thermal Conductivity of the Solidified Inert Gases: Argon, Neon, and Krypton, Philosophical Magazine, vol. 3, pp. 785-797, 1958.

29. F. Clayton and D. N. Batchelder, Temperature and Volume Dependence of the Thermal Conductivity of Solid Argon, Journal of Physics C: Solid State Physics, vol. 6, pp. 1213-1228, 1973.

30. Y. S. Touloukian, P. E. Liley and S. C. Saxena, eds., Thermal Conductivity: Nonmetallic Liquids and Gases, IFI/Plenum, New York, 1970.

31. G. J. Keeler and D. N. Batchelder, Measurement of the Elastic Constants of Argon from 3 to 77° K, Journal of Physics C: Solid State Physics, vol. 3, pp. 510-522, 1970.

32. H. B. G. Casimir, Note on the Conduction of Heat in Crystals, Physica, vol. 5, pp. 495-500, 1938.

33. P. G. Klemens, The Scattering of Low-Frequency Lattice Waves by Static Imperfections, Proceedings of the Physical Society of London, vol. 68, pp. 1113-1128, 1955.

34. R. Peierls, Zur kinetischen Theorie der Wärmeleitung in Kristallen, Annalen der Physik, vol. 3, pp. 1055-1101, 1929.

35. C. R. Havis, G. P. Peterson and L. S. Fletcher, Predicting the Thermal Conductivity and Temperature Distribution in Aligned Fiber Composites, Journal of Thermophysics and Heat Transfer, vol. 3, pp. 416-422, 1989.

36. A. L. Nayak and C.-L. Tien, A Statistical Thermodynamic Theory for Coordination-Number Distribution and Effective Thermal Conductivity of Random Packed Beds, International Journal of Heat and Mass Transfer, vol. 21, pp. 669-676, 1978.

37. J. Che, T. Çagin, W. Deng and W. A. Goddard III, Thermal Conductivity of Diamond and Related Materials from Molecular Dynamics Simulations, Journal of Chemical Physics, vol. 113, pp. 6888-6900, 2000.

38. S. Kotake and S. Wakuri, Molecular Dynamics Study of Heat Conduction in Solid Materials, JSME International Journal, Series B, vol. 37, pp. 103-108, 1994.

39. D. A. Young, C. Thomsen, H. T. Grahn, H. J. Maris and J. Tauc, Heat Flow in Glasses on a Picosecond Time Scale, in A.C. Anderson and J.P. Wolfe (eds.), Phonon Scattering in Condensed Matter V, pp. 49-51, Springer, Berlin, 1986.

40. W. A. Little, The Transport of Heat Between Dissimilar Solids at Low Temperatures, Canadian Journal of Physics, vol. 37, pp. 334-349, 1959.

41. E. T. Swartz and R. O. Pohl, Thermal Boundary Resistance, Reviews of Modern Physics, vol. 61, pp. 605-, 1989.

42. V. Lehmann, The Physics of Macroporous Silicon Formation, Thin Solid Films, vol. 255, pp. 1-4, 1995.

43. A.-P. Li, F. Müller, A. Birner, K. Nielsch and U. Gösele, Fabrication and Microstructuring of Hexagonally Ordered Two-Dimensional Nanopore Arrays in Anodic Alumina, Advanced Materials, vol. 11, pp. 483-487, 1999a.

44. R. Hérino, A. Perio, K. Barla and G. Bomchil, Microstructure of Porous Silicon and its Evolution with Temperature, Materials Letters, vol. 2, pp. 519-523, 1984.

Nomenclature

T^*	=	dimensionless temperature
x	=	cross-plane direction for thin film simulations
y	=	lateral coordinate
z	=	lateral coordinate

Greek symbol

ϕ_v	=	vacancy fraction

Figures

Figure 1 Computational configuration

Figure 2 Pore shapes in a single atomic x-plane near the center of a thin film at (a) the beginning and (b) the end of a simulation at $T^* = 0.50$

Figure 3 Dimensionless thermal conductivity versus dimensionless average lattice temperature for thin films with pores of various sizes

Figure 4 Atomic structure in central and adjacent x-planes in thin films at different temperatures and pore sizes

Figure 5 Pore configurations used in the simulations. Identifying labels are listed above each configuration

Figure 6 Normalized thermal conductivity versus vacancy fraction for various pore configurations at $T^* = 0.50$. Further details of these configurations are given in Figure 5

Figure 7 Temperature profiles for various pore positions within a film at $T^* = 0.17$

Figure 8 Dimensionless thermal boundary resistance induced by the pore and ratio of pore resistance to total thermal resistance of film

Figure 9 Effective thermal conductivity versus pore position

Figure 10 In-plane temperature contours and heat flux distributions for a film with a 5-vacancy pore in the 2nd regular x-plane: (a) 3rd y-plane, (b) 4th y-plane, (c) 5th y-plane, (d) 1st regular x-plane, (e) 2nd regular x-plane, and (f) 3rd regular x-plane

Figure 11 In-plane temperature contours and heat flux distributions for a film with a 5-vacancy pore in the 6th regular x-plane: (a) 3rd y-plane, (b) 4th y-plane, (c) 5th y-plane, (d) 5th regular x-plane, (e) 6th regular x-plane, and (f) 7th regular x-plane

Figure 12 In-plane temperature contours and heat flux distributions for a film with a 5-vacancy pore in the 10th regular x-plane: (a) 3rd y-plane, (b) 4th y-plane, (c) 5th y-plane, (d) 9th regular x-plane, (e) 10th regular x-plane, and (f) 11th regular x-plane

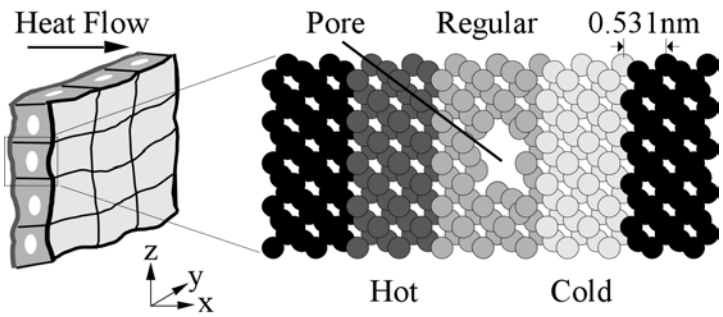

Figure 1 Computational configuration

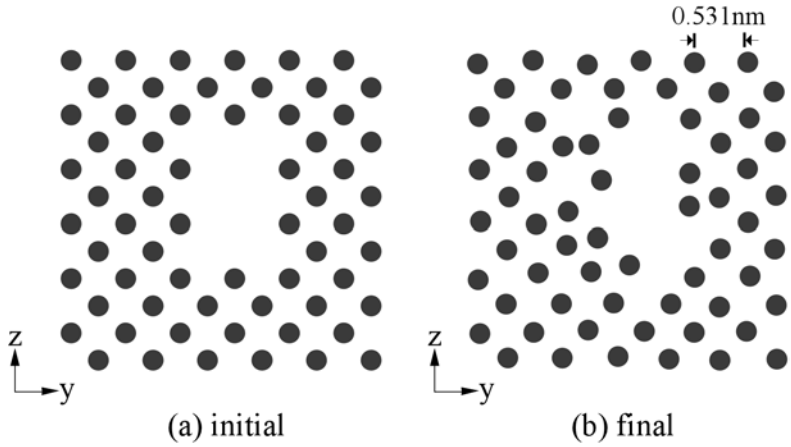

Figure 2 Pore shapes in a single atomic x-plane near the center of a thin film with 6x6 unit cell cross section at (a) the beginning and (b) the end of a simulation at $T^* = 0.50$

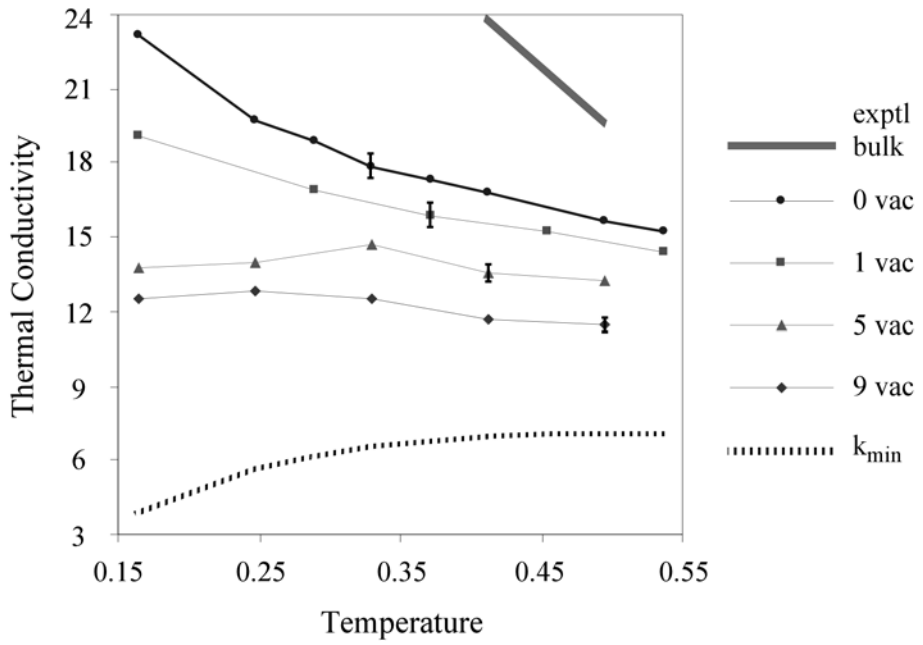

Figure 3 Dimensionless thermal conductivity versus dimensionless average lattice temperature for thin films with pores of various sizes

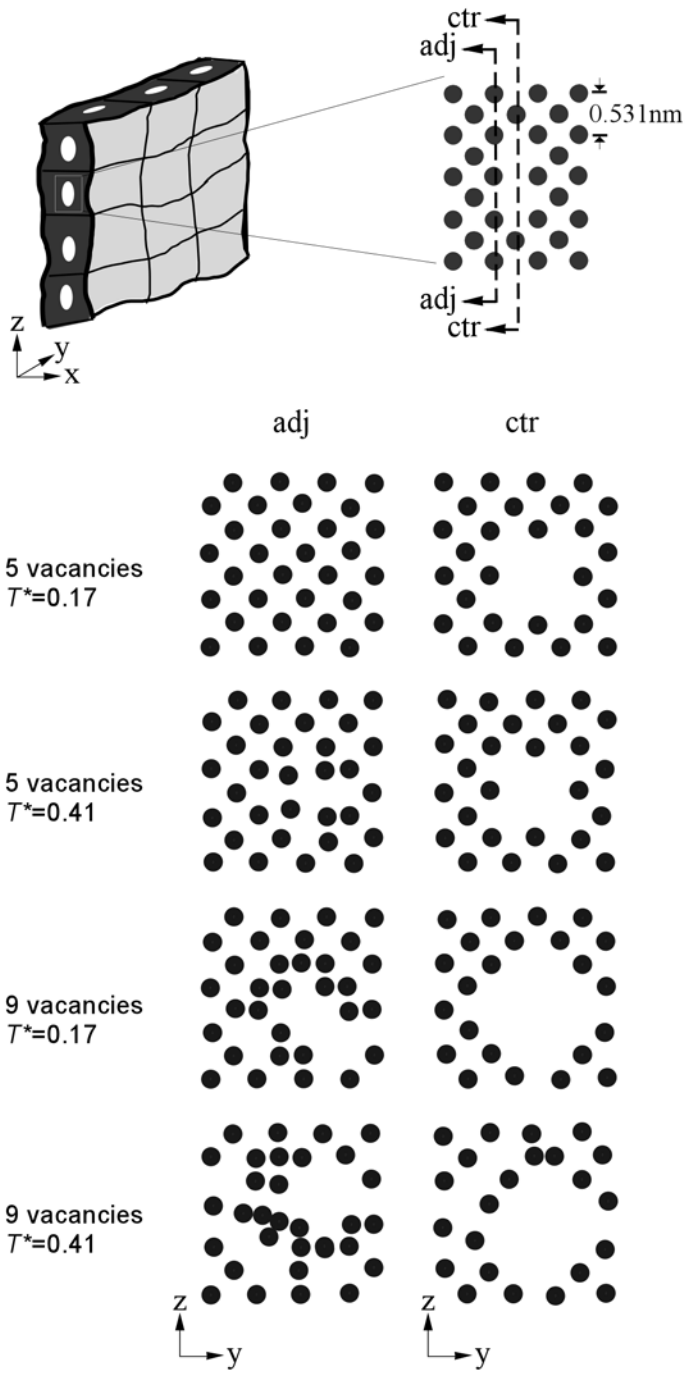

Figure 4 Atomic structure in central and adjacent x-planes in thin films at different temperatures and pore sizes

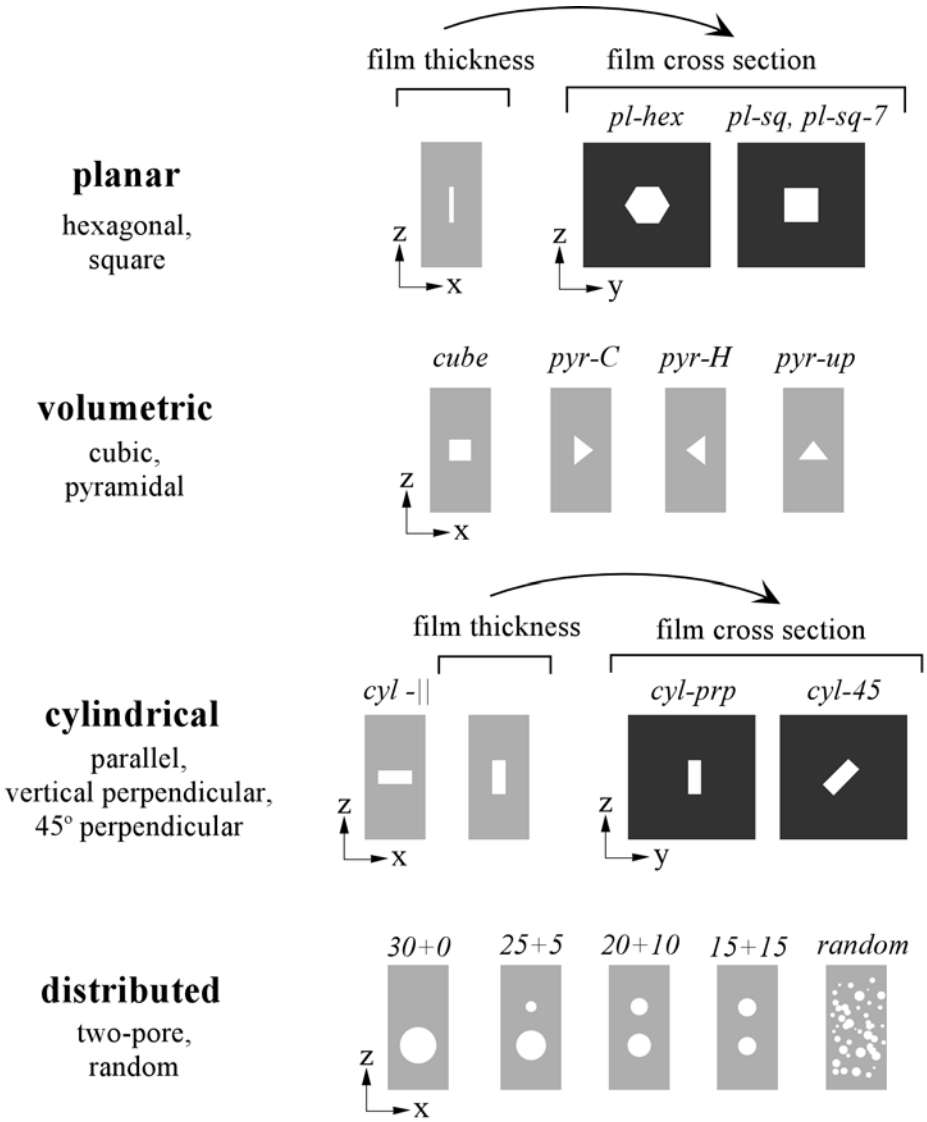

Figure 5 Pore configurations used in the simulations. Identifying labels are listed above each configuration

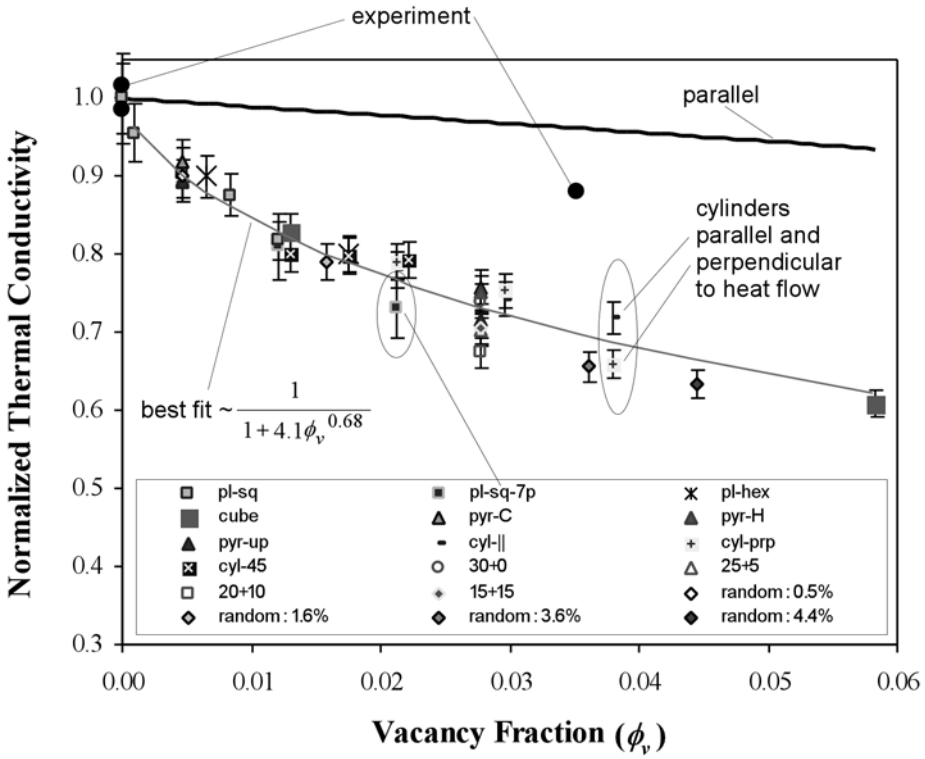

Figure 6 Normalized thermal conductivity versus vacancy fraction for various pore configurations at $T^* = 0.50$. Further details of these configurations are given in Figure 5

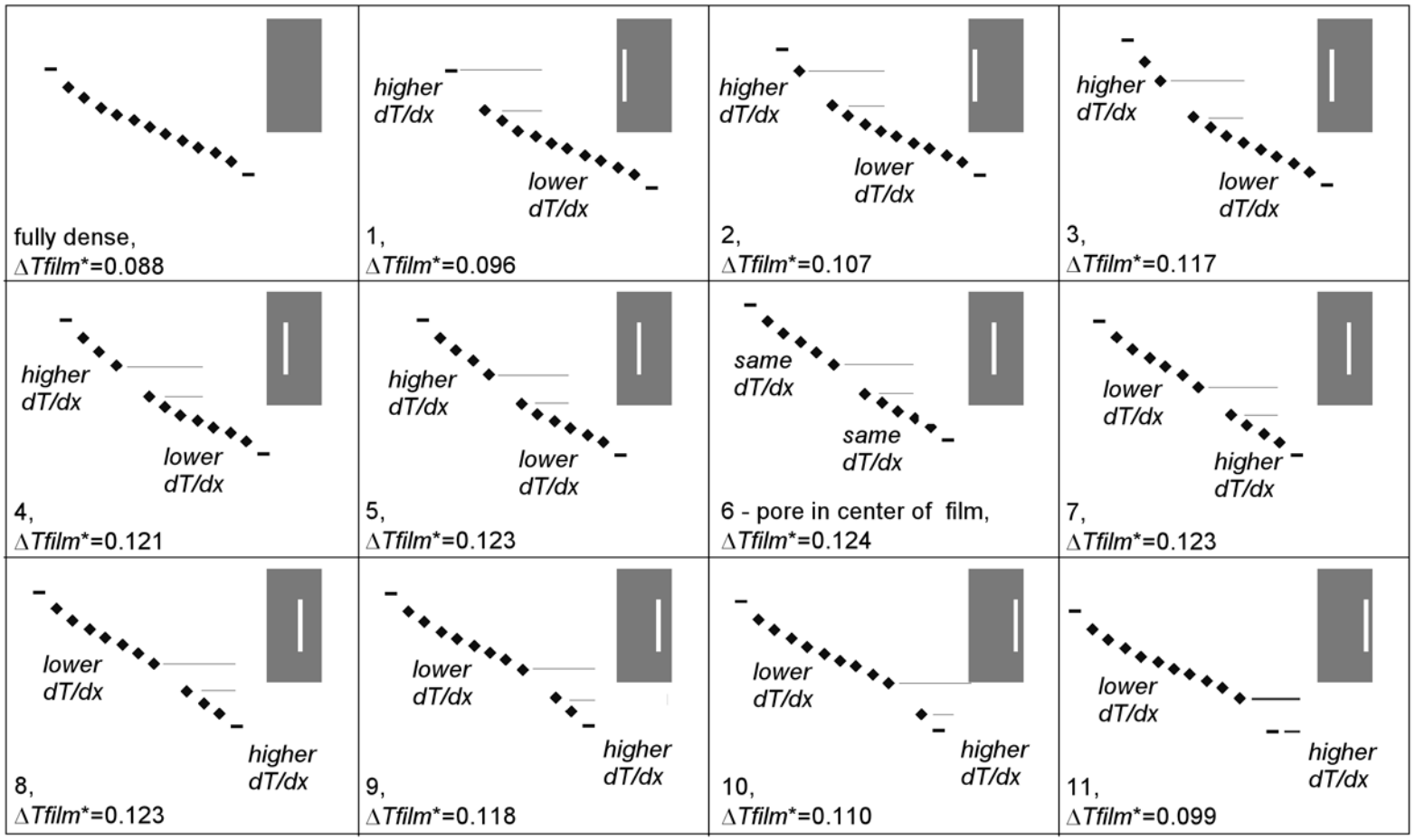

Figure 7 Temperature profiles for various pore positions within a film at $T^* = 0.17$

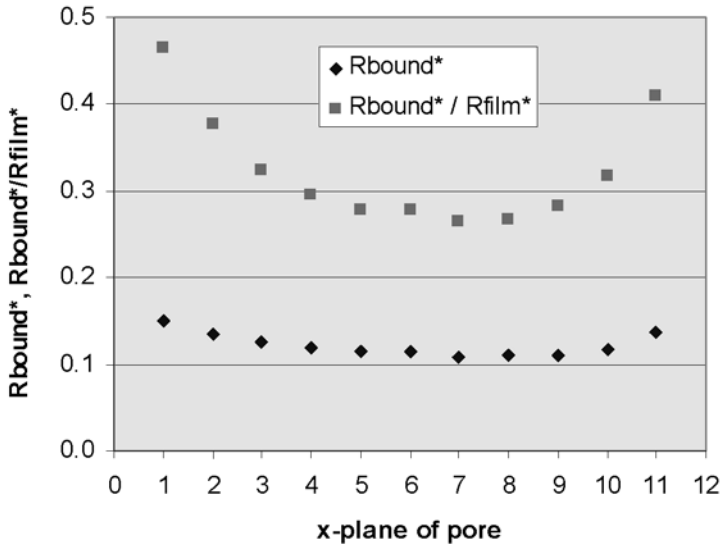

Figure 8 Dimensionless thermal boundary resistance induced by the pore and ratio of pore resistance to total thermal resistance of film

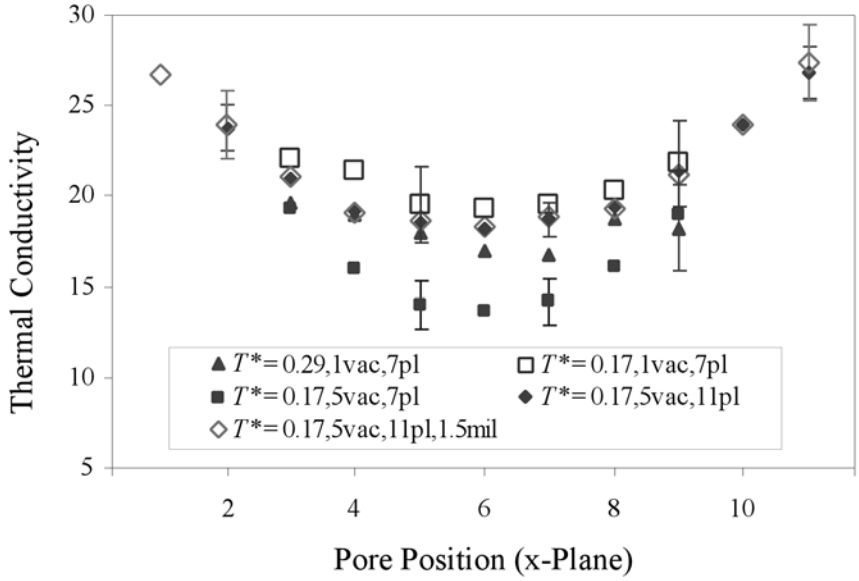

Figure 9 Effective thermal conductivity versus pore position

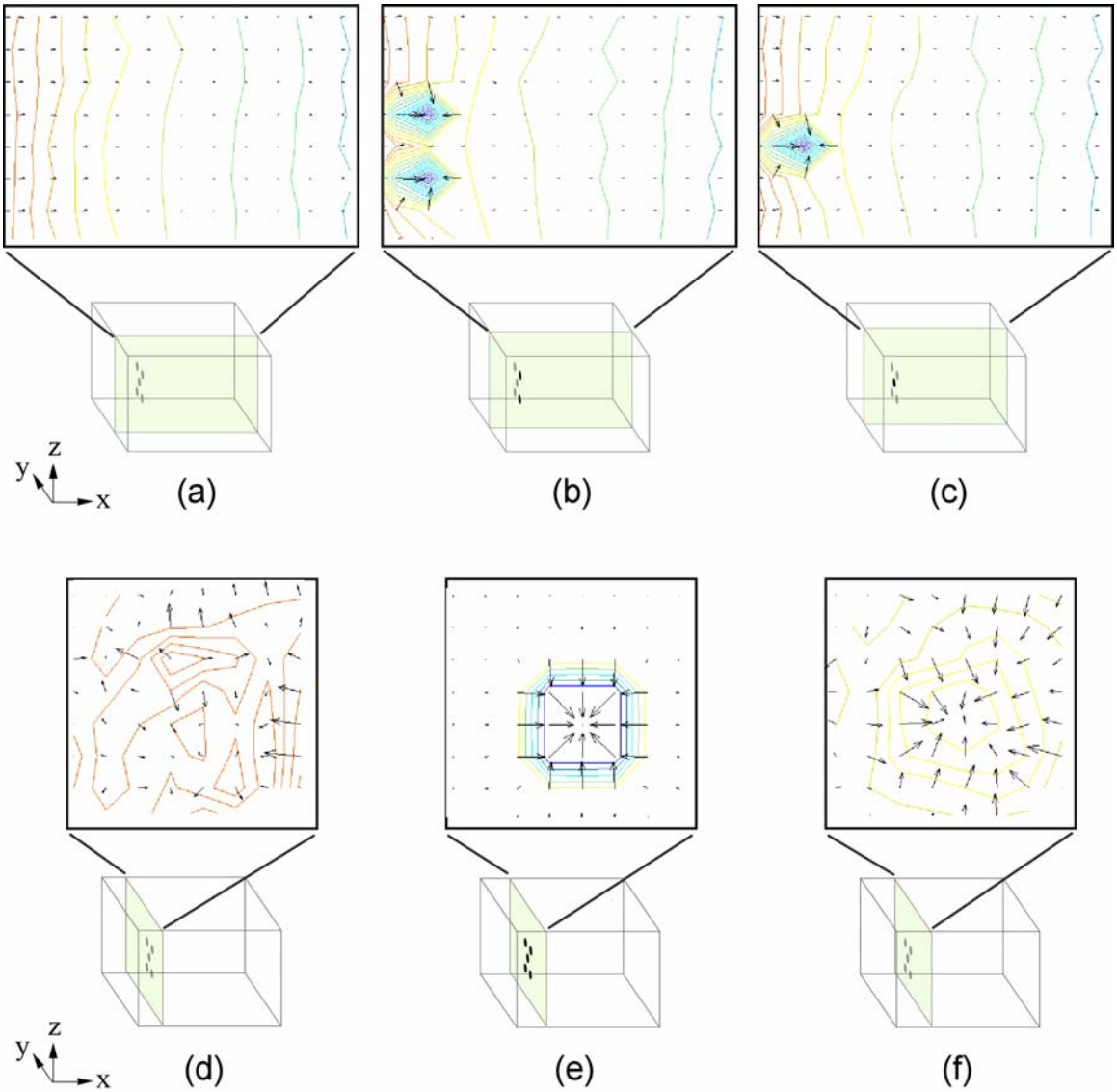

Figure 10 In-plane temperature contours and heat flux distributions for a film with a 5-vacancy pore in the 2nd regular x-plane: (a) 3rd y-plane, (b) 4th y-plane, (c) 5th y-plane, (d) 1st regular x-plane, (e) 2nd regular x-plane, and (f) 3rd regular x-plane

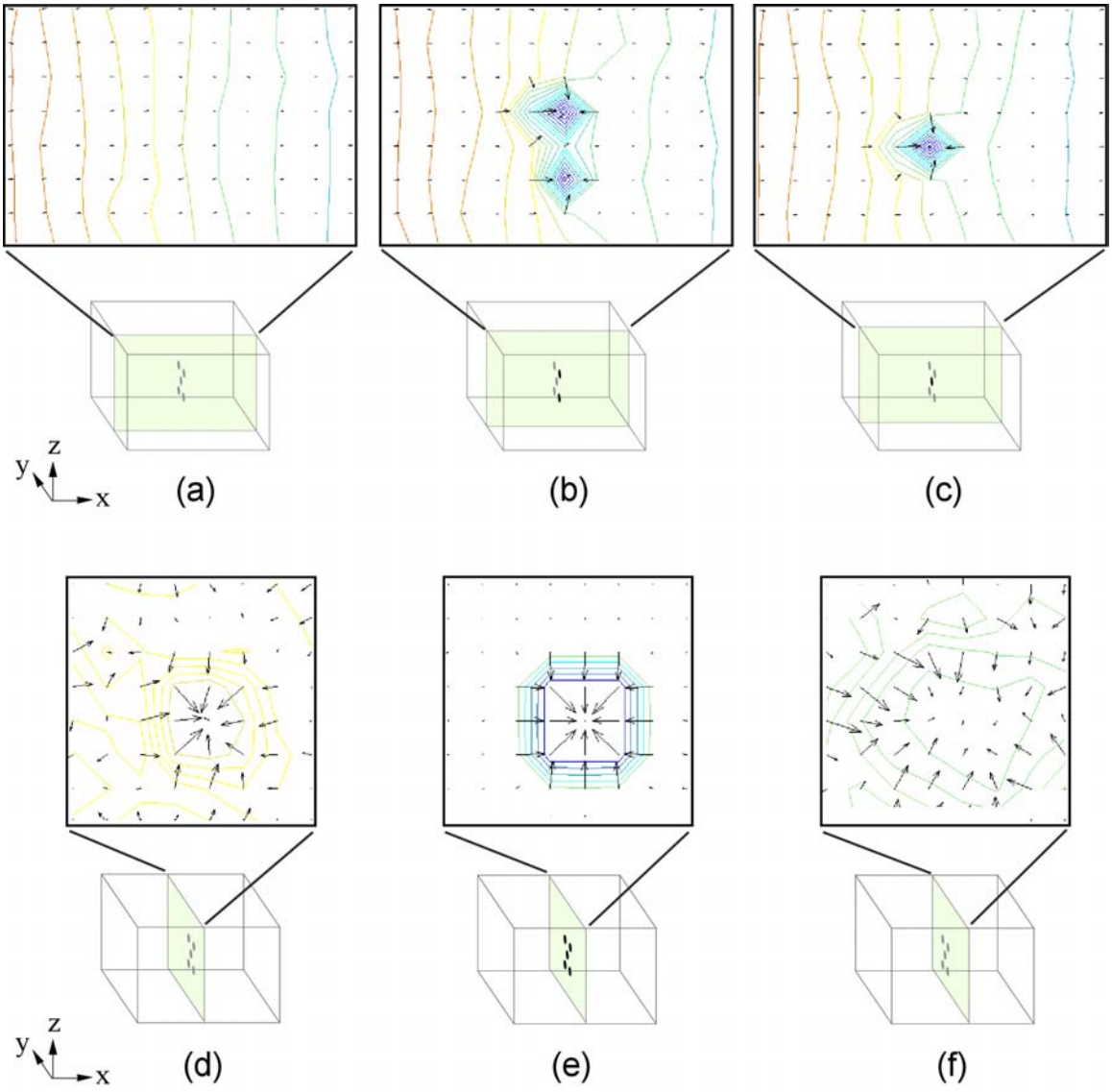

Figure 11 In-plane temperature contours and heat flux distributions for a film with a 5-vacancy pore in the 6th regular x-plane: (a) 3rd y-plane, (b) 4th y-plane, (c) 5th y-plane, (d) 5th regular x-plane, (e) 6th regular x-plane, and (f) 7th regular x-plane

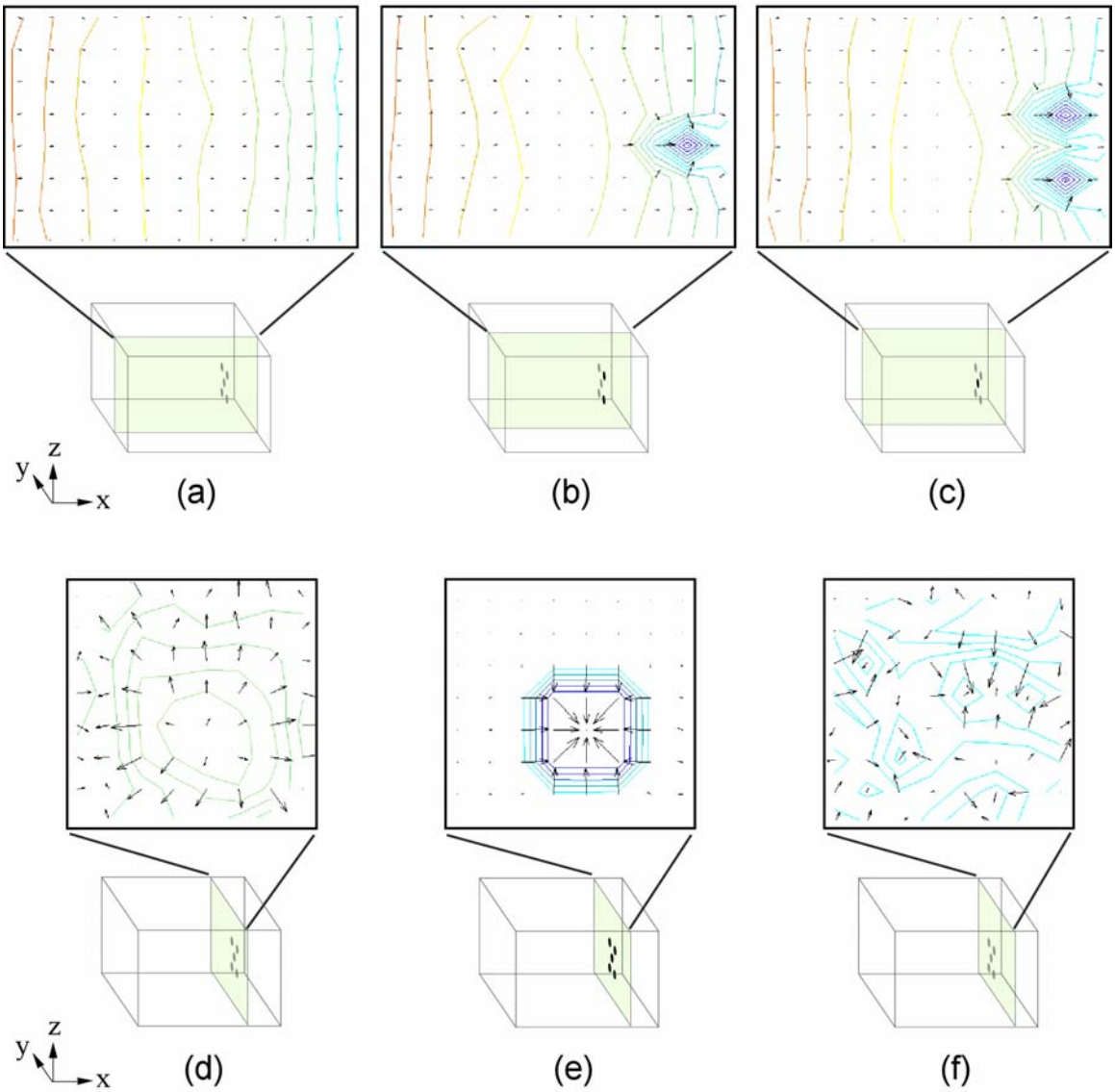

Figure 12 In-plane temperature contours and heat flux distributions for a film with a 5-vacancy pore in the 10th regular x-plane: (a) 3rd y-plane, (b) 4th y-plane, (c) 5th y-plane, (d) 9th regular x-plane, (e) 10th regular x-plane, and (f) 11th regular x-plane

Table 1 Simulation parameters and nondimensionalization equations

Time step	1 fs
Time step at which heat flux is applied	50,000
Time step at which time averaging begins	100,000
Total timesteps in simulation	0.5 – 3 million
Data sampling frequency	every 400 time steps
Atomic x-planes in each hot or cold region	4
Atomic x-planes in each fixed region	4
Number of regular x-planes[1]	7, 9, 11
Height x width of cross section in FCC unit cells (UC)	4x4, 6x6
Number of atoms per x-plane	32 (4x4), 72 (6x6)
Dimensionless spring constant value	10
Imposed dimensionless heat flux (J_Q^*)	0.3
Well depth parameter (ε_{LJ})	1.67×10^{-21} J
Equilibrium separation parameter (σ_{LJ})	0.34 nm
Atomic mass (m)	66.3×10^{-27} kg
Boltzmann's constant (k_B)	1.38×10^{-23} J/K
Lattice constant	0.531 nm
Dimensionless spring constant	$K^* = K \frac{\sigma_{LJ}^2}{\varepsilon_{LJ}}$
Dimensionless temperature	$T^* = \frac{k_B T}{\varepsilon_{LJ}}$
Dimensionless heat flux	$J_Q^* = J_Q \sigma_{LJ}^3 \sqrt{\frac{m}{\varepsilon_{LJ}^3}}$
Dimensionless thermal conductivity	$k^* = k \frac{\sigma_{LJ}^2}{k_B} \sqrt{\frac{m}{\varepsilon_{LJ}}}$

[1]Parameters for specific simulations have been varied as noted in text